Equation of state for CO and CO_2 fluids and its application on decarbonation reactions at high pressure and temperature

Yunguo Li[1]*, Lidunka Vočadlo[1], Amy Edgington[1] and John P. Brodholt[1,2]

[1]*Department of Earth Science, UCL, Gower Street, London, WC1E 6BT, UK*

[2]*Centre for Earth Evolution and Dynamics, University of Oslo, Oslo, Norway*

[*]Corresponding author: Yunguo Li (email: yunguo.li@ucl.ac.uk).

Abstract

Ab initio molecular dynamics simulations were performed at pressures and temperatures up to 160 GPa and 4000 K, in order to obtain equations of state (EOS) for CO and CO_2 fluids. We found that polymerisation of CO and CO_2 fluids starts at low pressures, and that including the effect of polymerisation is essential for accurate EOS. EOSs for CO and CO_2 determined from methods using experimental data, or classical potentials that ignore the changes in speciation, should be treated with caution when extrapolated beyond the examined pressures and temperatures. The obtained data was fitted into a modified Lee and Kesler EOS for both CO and CO_2 fluids. The thermodynamic calculations for the decarbonation reactions of both $MgCO_3$ and $CaCO_3$ using the derived CO_2 EOS reproduced the experimental data and theoretical calculations at low pressures. Both $MgCO_3$ and $CaCO_3$ pure phases are found to be stable in the upper mantle compared to CO_2. However, they both become destabilised when approaching lower mantle conditions.

Keywords

Decarbonation reaction; equation of state; CO_2 fluid; CO fluid; polymerisation; carbonate

1 Introduction

Accurate descriptions of P-V-T (Pressure-Volume-Temperature) data and thermal properties of CO and CO_2 fluids are needed for a complete and robust thermophysical description of the Earth's mantle. Such knowledge is also important for understanding the interiors of giant planets such as Neptune, Uranus and the many similar exoplanets that are composed of C, H, O and N under high pressures and temperatures (Cavazzoni et al., 1999; Hubbard, 1981). Furthermore, the fundamental questions on the evolution of molecular bonding with increasing pressure and temperature also prompt the study of CO and CO_2 at high P/T conditions (Bernard et al., 1998; Datchi et al., 2009; Iota et al., 2006; Santoro and Gorelli, 2006). The study of molecular fluids like CO and CO_2 under extreme conditions can not only help to understand their basic chemistry, but also is of general interest in materials science, geoscience and industry.

Significant effort has been devoted to the determination of the equations of state (EOS) and the properties of CO and CO_2 fluids under the conditions of planetary interiors. However, there are relatively few experimental data on CO and CO_2 fluids at high P/T conditions, with most studies at high P & T being theoretical. Belonoshko and Saxena used classical molecular dynamics (MD)

with a Buckingham potential to determine the EOS of volatile fluids (Belonoshko and Saxena, 1991a; Belonoshko and Saxena, 1992). They calculated the EOS of CO_2 fluid (BS-1992 EOS) in the range from 400 to 4000 K and from 0.5 to 100 GPa (Belonoshko and Saxena, 1992). Churakov and Gottschalk extended the EOS of CO_2 fluid (CG-2003 EOS) to 10000 K based on thermodynamic perturbation theory (Churakov and Gottschalk, 2003). Duan and Zhang obtained an EOS for CO_2 fluid (DZ-2006 EOS) based on *ab initio* calculations and experimental data from 0 GPa to 10 GPa and from 673 K to 2573 K (Duan and Zhang, 2006). Recently, Fu et al. (2017) formulated an EOS (FB-2017 EOS) based on several hundred *ab initio* molecular dynamics (AIMD) calculations performed between 0.5 and 104 GPa and from 600 to 4000 K for CO_2; they found substantial differences in EOS with some of the empirical potential results of Churakov and Gottschalk (2003) and Belonoshko and Saxena (1992). In the case of CO fluid, Belonoshko and Saxena derived an EOS of CO fluid (BS-1991 EOS), again using classical MD (Belonoshko and Saxena, 1991b). More recently, Leonhardi performed AIMD simulations to characterise CO fluid to 140 GPa and 5000 K and obtained an EOS (Leonhardi-2017 EOS; (Leonhardi and Militzer, 2017). Several shock-wave experiments exist on CO and CO_2, potentially allowing an assessment of the various EOSs, however little accurate temperature determination exists (Nellis et al., 1991; Nellis et al., 1981). Notably, in the shock experiments, CO and CO_2 molecules decomposed at high P and condensed into the diamond phase.

In this study, we perform AIMD simulations to determine the structural evolution and EOSs of CO and CO_2 fluids at temperatures from 1000 to 4000 K and pressures from 0 to 160 GPa. We find that pressure has little effect on the intramolecular C-O bond length in both CO and CO_2. Both CO and CO_2 fluids exhibit increased polymerisation from low pressures to high pressures, which is due to the pressure-induced intermolecular bonding. We show convincingly that polymerisation is a pressure driven process. The change of speciation of CO and CO_2 fluids by polymerisation suggests results in the literature based on classical methods or extrapolation from experimental data need to be re-evaluated. We apply the derived EOS to decarbonation reactions of $MgCO_3$ and $CaCO_3$, and obtain results which agree well with experimental data at low pressures.

2 Methods

2.1 AIMD simulations at high P/T conditions

We performed Born–Oppenheimer AIMD calculations based on density functional theory (DFT). We used the VASP code (Blöchl, 1994; Kresse and Joubert, 1999), PAW potentials (Kresse and Furthmüller, 1996; Kresse and Hafner, 1993) (with valence configurations $2s^2 2p^2$ and $2s^2 2p^4$ for C and O, respectively) and a planewave cut-off of 500 eV. We used a supercell containing 64 molecules for both CO_2 and CO. The Brillouin zone was sampled with the Γ-point. This setting converged the pressure to within 0.2 GPa. Exchange-correlation effects were treated in the generalized gradient approximation (GGA) with the Perdew-Burke-Ernzerhof (PBE) (Perdew et al., 1996) scheme. Single particle orbitals were populated according to the Fermi–Dirac statistics. The integration (with the time step of 1.0 fs) of the classical Newton's equations of motion uses the Verlet algorithm, and the ground-state search is done within an efficient iterative matrix diagonalization scheme and a Pulay mixer for each step. We ran NVT simulations at the target temperatures and pressures; the temperature was controlled by a Nosé thermostat (Di Tolla and Ronchetti, 1993; Nosé, 1984); these simulations were run for over 5 ps and up to 30 ps depending on the equilibration time. Stresses were averaged from NVT calculations within the production period of at least 3 *ps*. The input structures were carefully prepared using the Packmol code (Martínez et al., 2009), in which the intermolecular distances (>1.6 Å) are larger than the intramolecular bond lengths.

2.2 EOS for CO and CO_2 fluids

For CO and CO_2 fluids, the calculated P-V-T data were fitted into the Lee and Kesler equation (Lee Byung and Kesler Michael, 1975) modified by Duan and Zhang (2006)

$$\frac{PV}{RT} = \mathbf{1} + \frac{B}{V_r} + \frac{C}{V_r^2} + \frac{D}{V_r^4} + \frac{E}{V_r^5} + \frac{F}{V_r^2}\left(\boldsymbol{\beta} + \frac{\gamma}{V_r^2}\right) \boldsymbol{exp}\left(-\frac{\gamma}{V_r^2}\right) \qquad (1)$$

where

$$\boldsymbol{V_r} = \frac{V}{V_C} \qquad (2)$$

$$\boldsymbol{B} = \boldsymbol{a_1} + \frac{a_2}{T_r^2} + \frac{a_3}{T_r^3} \qquad (3)$$

$$\boldsymbol{C} = \boldsymbol{a_4} + \frac{a_5}{T_r^2} + \frac{a_6}{T_r^3} \qquad (4)$$

$$\boldsymbol{D} = \boldsymbol{a_7} + \frac{a_8}{T_r^2} + \frac{a_9}{T_r^3} \qquad (5)$$

$$\boldsymbol{E} = \boldsymbol{a_{10}} + \frac{a_{11}}{T_r^2} + \frac{a_{12}}{T_r^3} \qquad (6)$$

$$\boldsymbol{F} = \frac{\boldsymbol{\alpha}}{\boldsymbol{T_r^3}} \quad (7)$$

$$\boldsymbol{T_r} = \frac{\boldsymbol{T}}{\boldsymbol{T_C}} \quad (8)$$

R is the gas constant; T is the temperature and V is the volume; V_C and T_C are the critical volume and temperature, respectively; a_1 to a_{12}, α, β and γ are fitting parameters.

2.3 Thermodynamic calculation of decarbonation reactions

We applied the derived EOS of CO_2 fluid to the following decarbonation reactions:

(***R1***) $$\mathrm{MgCO_3 = MgO + CO_2},$$

(***R2***) $$\mathrm{MgCO_3 + SiO_2 = MgSiO_3 + CO_2},$$

(***R3***) $$\mathrm{CaCO_3 = CaO + CO_2},$$

(***R4***) $$\mathrm{CaCO_3 + SiO_2 = CaSiO_3 + CO_2}.$$

The Gibbs free energy of formation from the elements at a pressure and temperature is given by

$$G_{p,T} = G^{\circ}_{f(1\ \mathrm{bar},\,T)} + \int_{1\ \mathrm{bar}}^{p} V_T(p)dp$$

$$= \mathrm{H}^{\circ}_{f(1\ \mathrm{bar},\,298\ \mathrm{K})} - TS^{\circ}_{f(1\ \mathrm{bar},\,298\ \mathrm{K})} + \int_{1\ bar,\,298\ K}^{T} C_{p(1\ \mathrm{bar})}(T)dT - T\int_{1\ \mathrm{bar},\,298\ \mathrm{K}}^{T} C_{p(1\ \mathrm{bar})}(T)/TdT + \int_{1\ \mathrm{bar},T}^{P} V_T(p)dp \quad (9)$$

where $G^{\circ}_{f(1\ \mathrm{bar},\,T)}$ is the Gibbs free energy of formation at 1 bar and T, $\mathrm{H}^{\circ}_{f(1\ \mathrm{bar},\,298\ \mathrm{K})}$ and $\mathrm{S}^{\circ}_{f(1\ \mathrm{bar},\,298\ \mathrm{K})}$ are the standard enthalpy and entropy of formation, respectively; $C_{p(1\ \mathrm{bar})}$ is the isobaric specific heat capacity at 1 bar and $V_T(p)$ is the volume at p under constant T.

By using the EOS of CO_2 fluid obtained above, the Gibbs free energy at specific P & T can be calculated with the available experimental $G^{\circ}_{f(1\ \mathrm{bar},\,T)}$. For the minerals involved in the decarbonation reactions, we used existing EOS from the literature, except for magnetite where we refitted the PVT data to encompass a volume dependent Anderson-Grüneisen parameter δ_T. In Table S1, we list the thermodynamic quantities taken from literature.

Specifically, we used a high temperature Birch-Murnaghan (HTBM) EOS for both $MgCO_3$ and MgO, following (Redfern et al., 1993). The third-order BM EOS is given by

$$P(V) = \frac{3B_0}{2}\left[\left(\frac{V_0}{V}\right)^{7/3} - \left(\frac{V_0}{V}\right)^{5/3}\right]\left\{1 + \frac{3}{4}(B_0' - 4)\left[\left(\frac{V_0}{V}\right)^{2/3} - 1\right]\right\} \quad (10)$$

where B_0, V_0 and B_0' are the isothermal bulk modulus, equilibrium volume and pressure derivative of B_0 to pressure at ambient conditions, respectively. The temperature dependence of volume is described by using the volume-dependent Anderson-Gruneisen parameter δ_T

$$\delta_T = -\left(\frac{1}{\alpha B_T}\right)\left(\frac{\partial B_T}{\partial T}\right)_P = \left(\frac{\partial \ln(\alpha)}{\partial \ln(V)}\right)_T = \frac{V}{V_0}\cdot m - 1 \quad (11)$$

where α is the volumetric thermal expansion coefficient, and m is a dimensionless parameter (Chopelas and Boehler, 1992).

For $MgSiO_3$, SiO_2, $CaCO_3$ (*aragonite*, *arag*), CaO and $CaSiO_3$, we used the form of HTBM used by Dubrovinsky and Swamy (1997); Litasov et al. (2008); Litasov et al. (2017); Oda et al. (1992); Swamy et al. (1994); Tange et al. (2012). In this form, B_0, V_0 and B_0' all become temperature dependent. The temperature dependence of the equilibrium volume is expressed by α

$$V_{1\ bar,\ T} = V_{1\ bar,\ 298.15\ K}\, exp\left(\int_{298.15\ K}^{T} \alpha dT\right) \quad (12)$$

and the temperature dependence for B_0 and B_0' is defined by $(\partial B_0/\partial T)_p$ and $(\partial B_0'/\partial T)_p$. respectively.

For other phases of $CaCO_3$, we used the data produced by *ab initio* calculations from Zhang et al. (2018). The second form of HTBM was used to describe the EOSs under 900 K, and a Mie-Gruneisen EOS was used for temperatures over 900 K, according to Zhang et al. (2018). Details can be found in the original publication.

3 Results

3.1 Structure and polymerisation of CO and CO_2 fluids at high P/T conditions

AIMD simulations were performed at temperatures of 1000, 2000, 3000 and 4000 K for both CO and CO_2, and at densities of 0.5 to 4.5 g/cm^3. We expect from these simulations that not only the speciation of CO and CO_2 at high P/T conditions can be obtained, but also, we can better understand the evolution of molecular bonding with increasing pressure and temperature.

We analysed MD trajectories to obtain the structural information and extract the speciation information. We calculated the radial distribution function (RDF) for each atom in the system. The calculated RDFs for CO and CO_2 fluids are shown in Figures 1 and 2 (and in Supplementary

Materials (**SM**)), and the speciation of CO and CO_2 fluids is shown in Table 1. We collected the average pressure for each run and the results are also shown in Table 1.

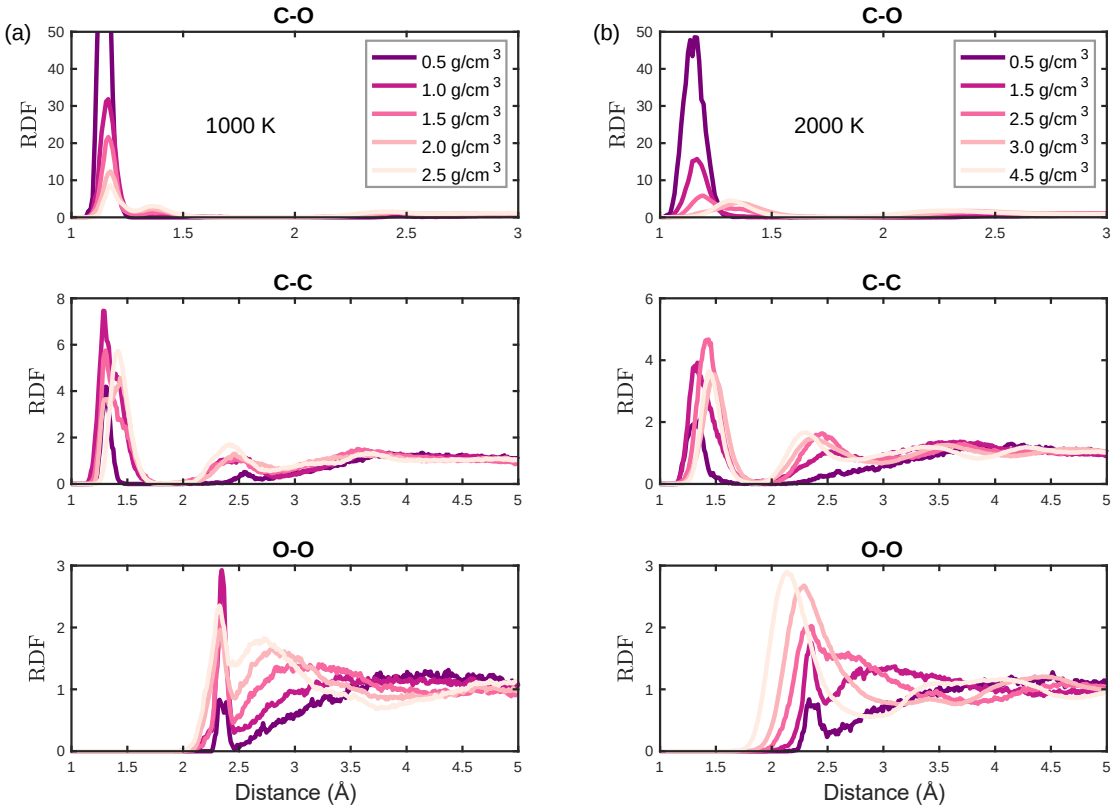

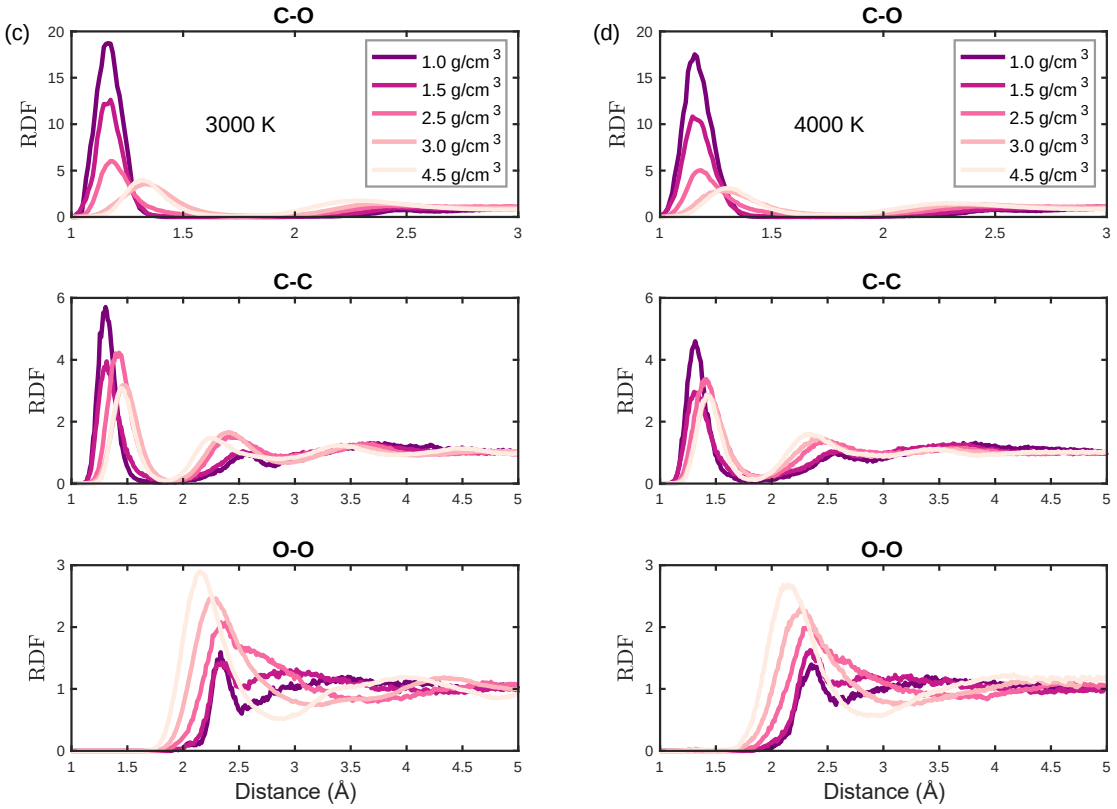

Figure 1. Calculated radial distribution functions (RDFs) in CO fluid at 1000, 2000, 3000 and 4000 K under different densities (pressures). The main C-O peak at *ca.* 1.17 Å belongs to CO and CO_2 molecules. The C-C peaks at *ca.* 1.37 Å and 2.48 Å indicate the polymerisation of CO fluid.

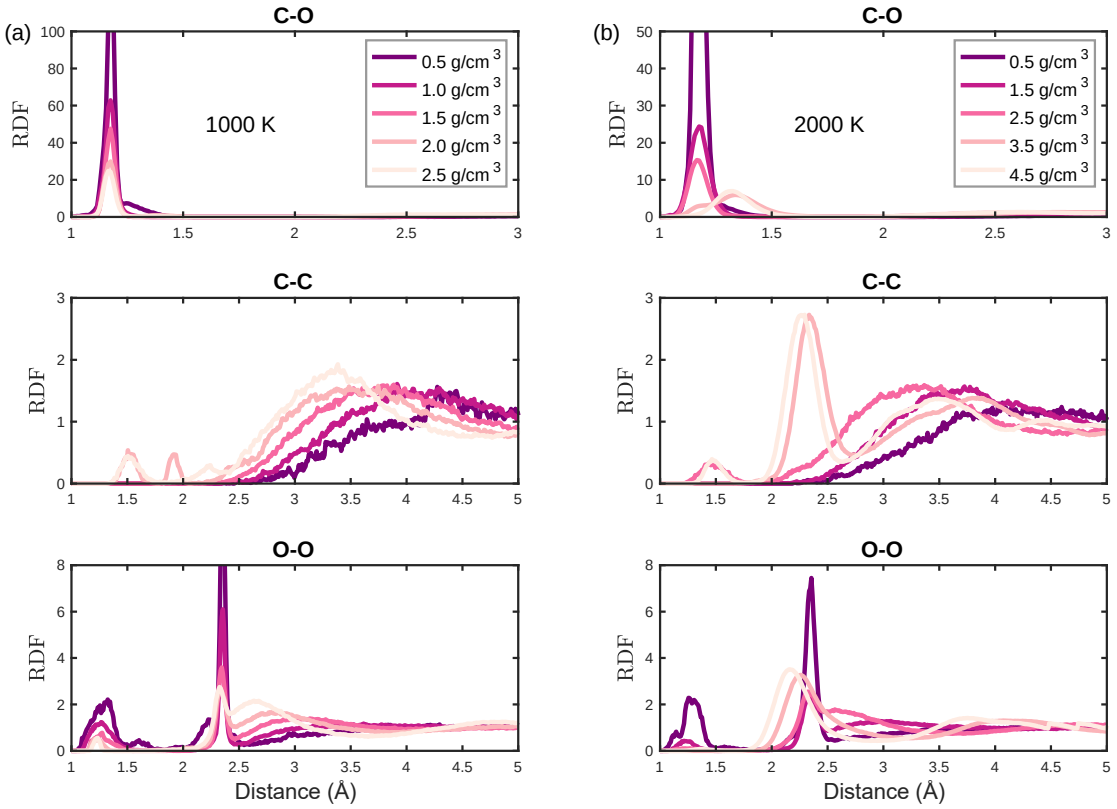
(a)
(b)
C-O
C-C
O-O
RDF
1000 K
2000 K
0.5 g/cm 3
1.0 g/cm 3
1.5 g/cm 3
2.0 g/cm 3
2.5 g/cm 3
3.5 g/cm 3
4.5 g/cm 3
Distance (Å)

145

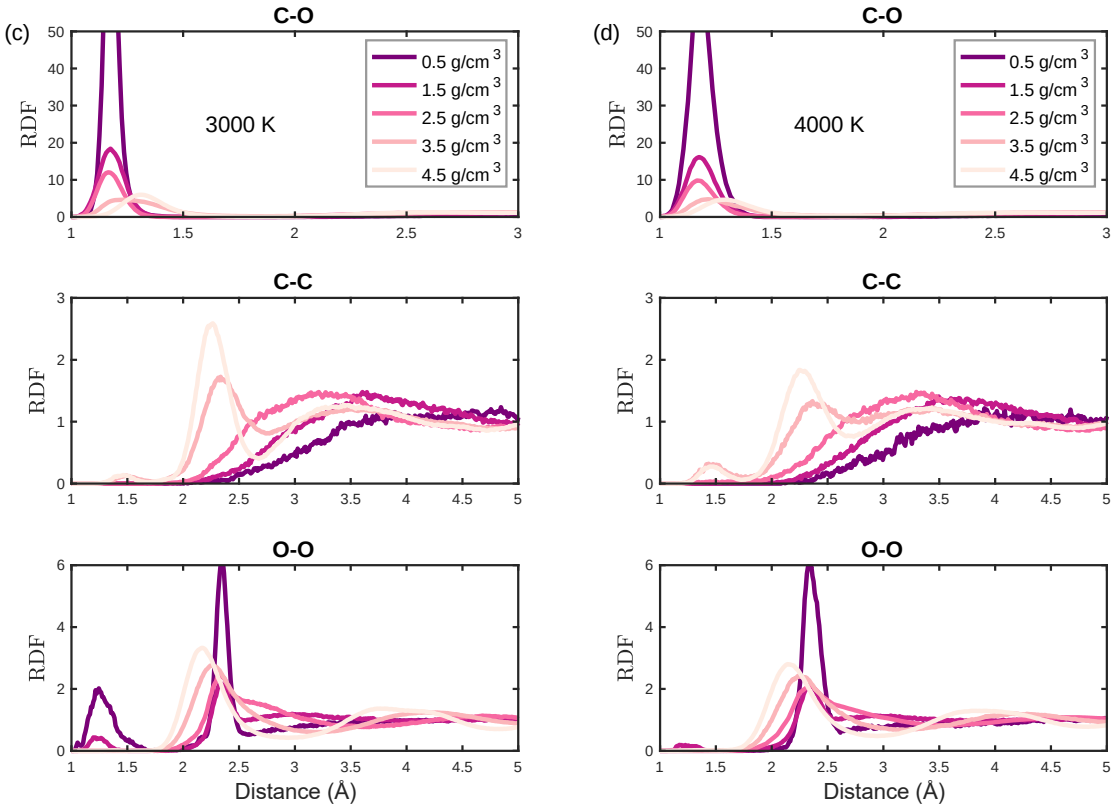

Figure 2. Radial distribution functions in CO_2 fluid at 1000, 2000, 3000 and 4000 K under different densities (pressures). The main C-O peak at *ca.* 1.17 Å belongs to CO and CO_2 molecules. The C-C peaks at *ca.* 1.41 Å and 2.48 Å indicate the polymerisation of CO fluid. The O-O peak at ca. 1.25 Å corresponds to the bond length in the O_2 molecule.

Table 1. Calculated P-V-T data and the population of different species. The calculation of molecular CO, CO_2 and polymerised C populations is based on the total C budget of the system, and the calculation of molecular O_2 population is based on the O budget of the system.

Fluid	Temperature (K)	Perssure (GPa)	Volume (cm^3/mol)	Desntity (g/cm^3)	Population (%)			
					CO	CO_2	O_2	Polymerised C
CO	1000 K	0.27	56.02	0.5	89.06	3.13	0.00	7.81
	1000 K	1.00	28.01	1.0	38.91	16.72	0.00	44.38
	1000 K	3.86	18.67	1.5	24.22	15.31	0.00	60.47
	1000 K	8.20	14.00	2.0	8.59	11.72	0.00	79.69
	1000 K	15.25	11.20	2.5	2.03	10.78	0.00	87.19
	2000 K	0.48	56.02	0.5	83.59	2.97	0.00	13.44
	2000 K	1.93	28.01	1.0	37.81	16.09	0.00	46.09
	2000 K	5.88	18.67	1.5	23.13	13.13	0.00	63.75
	2000 K	10.54	14.00	2.0	7.81	13.28	0.00	78.91
	2000 K	18.16	11.20	2.5	0.16	6.25	0.00	93.59

	2000 K	29.58	9.34	3.0	0.00	0.00	0.00	100
	2000 K	49.39	8.00	3.5	0.00	0.00	0.00	100
	2000 K	147.64	6.22	4.5	0.00	0.00	0.00	100
	3000 K	2.56	28.01	1.0	37.66	12.97	0.00	49.38
	3000 K	7.62	18.67	1.5	20.47	12.34	0.00	67.19
	3000 K	12.55	14.00	2.0	3.44	13.59	0.00	82.97
	3000 K	23.26	11.20	2.5	0.31	6.56	0.00	93.13
	3000 K	37.65	9.34	3.0	0.00	2.50	0.00	97.50
	3000 K	55.07	8.00	3.5	0.00	0.00	0.00	100
	3000 K	149.61	6.22	4.5	0.00	0.00	0.00	100
	4000 K	3.27	28.01	1.0	34.84	11.41	0.00	53.75
	4000 K	8.33	18.67	1.5	17.03	10.16	0.00	72.81
	4000 K	25.82	11.20	2.5	0.63	4.53	0.00	94.84
	4000 K	42.04	9.34	3.0	0.00	0.78	0.00	99.22
	4000 K	67.39	8.00	3.5	0.00	0.00	0.00	100.00
	4000 K	160.53	6.22	4.5	0.00	0..00	0.00	100.00
CO_2	1000 K	0.10	88.02	0.5	30.00	64.38	3.67	5.63
	1000 K	0.91	44.01	1.0	27.66	70.78	9.92	1.56
	1000 K	3.75	29.34	1.5	16.09	79.69	2.11	4.22
	1000 K	9.58	22.00	2.0	11.56	72.97	2.27	15.47
	1000 K	22.21	17.60	2.5	1.82	64.12	9.38	34.06
	1000 K	49.19	12.57	3.5	0.00	3.20	69.16	96.80
	2000 K	0.38	88.02	0.5	24.83	72.58	5.79	2.60
	2000 K	1.44	44.01	1.0	26.10	70.26	3.86	3.64
	2000 K	4.53	29.34	1.5	15.31	78.91	3.05	5.78
	2000 K	12.56	22.00	2.0	3.82	80.80	2.25	15.35
	2000 K	25.62	17.60	2.5	1.88	64.06	1.56	34.06
	2000 K	39.63	14.67	3.0	0.00	2.74	2.16	97.26
	2000 K	50.67	12.57	3.5	0.00	1.66	0.00	98.34
	2000 K	85.68	11.00	4.0	0.00	0.00	8.13	100
	2000 K	132.94	9.78	4.5	0.00	0.00	0.00	100
	3000 K	0.64	88.02	0.5	24.53	75.47	2.16	0.00
	3000 K	2.24	44.01	1.0	25.69	62.36	5.95	11.95
	3000 K	5.95	29.34	1.5	12.81	64.84	3.28	22.34
	3000 K	14.31	22.00	2.0	3.75	53.91	1.95	42.34
	3000 K	29.02	17.60	2.5	1.09	32.03	0.70	66.88
	3000 K	46.50	14.67	3.0	0.94	14.84	0.16	84.22
	3000 K	50.67	12.57	3.5	0.00	0.00	0.00	100

3000 K	90.75	11.00	4.0	0.00	0.00	0.00	100
3000 K	132.94	9.78	4.5	0.00	0.00	0.00	100
4000 K	0.72	88.02	0.5	0.82	90.74	0.00	8.44
4000 K	6.86	29.34	1.5	10.16	72.03	2.11	17.81
4000 K	15.94	22.00	2.0	6.72	54.69	2.34	38.59
4000 K	30.83	17.60	2.5	1.56	39.22	0.39	59.22
4000 K	48.21	14.67	3.0	0.59	17.24	0.35	82.17
4000 K	71.08	12.57	3.5	0.31	4.69	0.16	95.00
4000 K	103.61	11.00	4.0	0.00	0.00	0.43	100
4000 K	151.80	9.78	4.5	0.00	0.00	0.00	100

The RDFs for CO fluid in Figure 1 clearly show that the main C-O peak at *ca*. 1.17 Å is continuously weakened with the increasing density/pressure at all temperatures, but the position of the peak remains almost the same. At the same time, a shoulder peak at *ca*. 1.36 Å starts to appear. This arising peak corresponds to the C-O bond in the polymerised segments. The change of C-O peaks suggests the continuous dissociation of CO molecules due to the establishment of intermolecular bonding and the stability of C-O intramolecular bonding character with increasing pressure. Also, in Figure 1, we can see the growth of a C-C peak at *ca*. 1.37 Å, which suggests the direct bonding between C atoms of neighbouring CO molecules. Both the C-C peak at *ca*. 1.37 Å and C-O peak at *ca*. 1.36 Å belong to the polymerised segments. With increasing pressure, a second C-C peak at *ca*. 2.48 Å also becomes more and more prominent, and at about the same position an O-O peak also becomes more evident. These two peaks correspond to the C-X-C (X denotes C or O) and O-C-O bond lengths, respectively. There is no O-O peak at the O-O bond length (1.21 Å in the gas state) of O_2 molecules. We calculated the population of different species at different P/T conditions by averaging their occurrences over time, which is listed in Table 1. We can see that the population of CO molecules decreased from 89.06% to 2.03% from 0.27 GPa to 15.25 GPa at 1000 K. CO_2 molecules immediately appeared even at 0.27 GPa, which accounts for only 3.13% of the total C budget. The population of CO_2 molecules quickly increased to its peak value of 16.72% at 1.00 GPa and then decreased with increasing pressure. The situation at other temperatures are similar to those at 1000 K. The population of polymerised C continuously increased with the increasing pressure, which reached up to 100% at 67.39 GPa and 4000 K. The solidified structure (see Figure S3 in **SM**) contains tetrahedrally coordinated C and O. Specifically, it contains diamond-like motifs, CO_4 tetrahedra and the intermediate mixtures of these two units.

From the CO_2 phase diagram, we can see that the thermodynamically stable phase at the range of 35 to 60 GPa is a quartz-like CO_2-V that is composed of CO_4 tetrahedra. The solidified structure of CO suggests that the stable phases could be diamond and CO_2-V when the fluids crystallise.

We perform a similar analysis on CO_2 fluid. As with CO fluid, the intensity of the main C-O peak at *ca*. 1.17 Å continuously decreases with increasing pressure at all temperatures, while the position of the peak remains almost the same, as can be seen in Figure 2. This reconfirms the finding in CO fluid that the intermolecular bonding will be gradually established while the intramolecular bonding remains the same under increasing pressure. In Figure 2, we can also see a C-C peak at *ca.* 1.48 Å that corresponds to the C-C direct bonding and a second C-C peak at *ca*. 2.41 Å that corresponds to the C-X-C bond. Together with the O-O peak at *ca*. 2.29 Å, this suggests the polymerisation of CO_2 fluid. One difference from the CO fluid is that there is an additional C-C peak at *ca*. 1.93 Å at 1000 K and 2.0 g/cm^3 (9.58 GPa). This peak corresponds to the C-C bond length in a very special molecule C_3O_6 (coordinates listed in Table S2 in **SM**), unique to this P/T condition and, as far as we are aware, not seen before in the literature. An O-O peak appears at *ca*. 1.25 Å at low pressures that belongs to O_2 molecules, which was not seen in CO fluids. From the population of different species in CO_2 fluid listed in Table 1, we can see that the population of CO_2 molecules generally drops with increasing pressure. There is a considerable concentration of CO molecules at low pressures; the CO population is 30% at 0.10 GPa and 1000 K, but it decreases with increasing pressure and drops to an insignificant amount at high pressures. O_2 molecules existed in CO_2 fluid at all conditions but never in a significant amount. The population of polymerised C continuously increased with the increasing pressure, and 92.19% CO_2 molecules were polymerised at 71.08 GPa and 4000 K. However, the structure was not solidified, even with 92.19% polymerisation, and the fluid is mainly composed of -C-O-C- chains and CO_4 tetrahedra (see Figure S3 in **SM**). Some molecules and -C-C-C- chains also exist.

We find a common phenomenon shared by both CO and CO_2 fluids that polymerisation proceeds as a result of the establishment of intermolecular bonding and the intramolecular bonding is hardly affected. The number of the original intramolecular bonds in CO and CO_2 molecules are reduced with the polymerisation, but the bond lengths of the remaining intact CO and CO_2 molecules hardly change. We plot the population of polymerisation in the P-T phase diagram in Figures 3 and 4, which show clearly that polymerisation is mainly dependent on pressure.

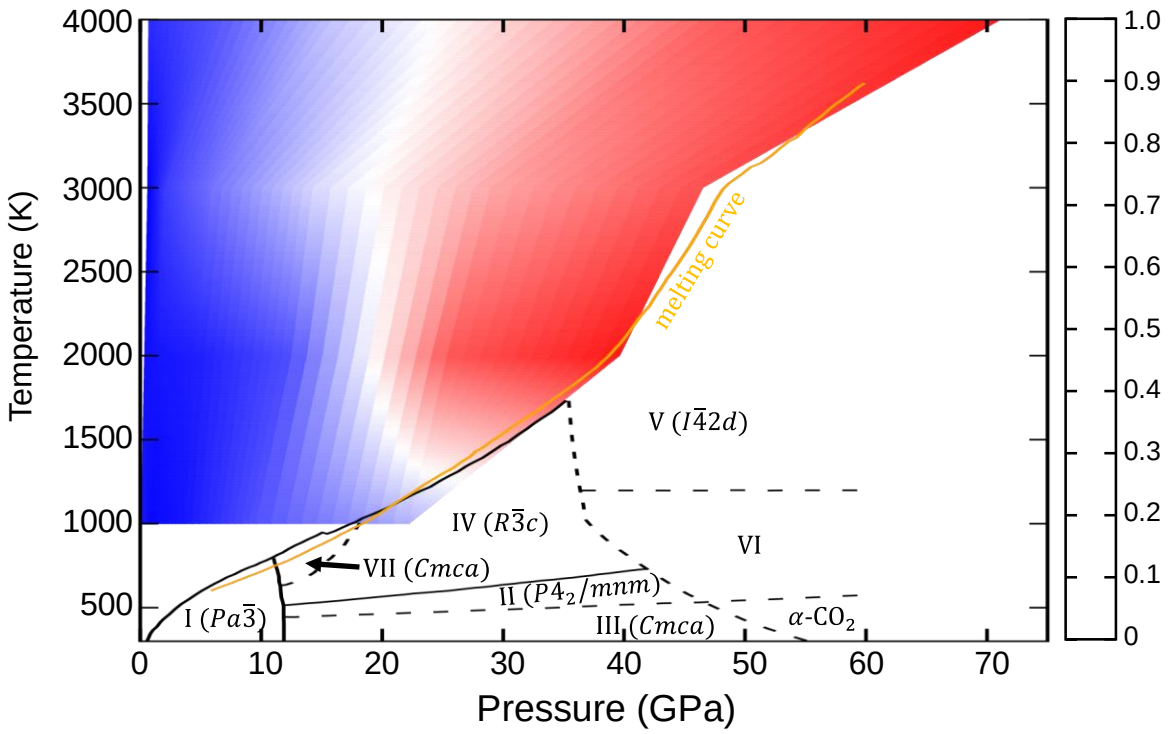

Figure 3. P-T phase diagram of CO_2. The black and orange lines show phase boundaries from the literature (Giordano and Datchi, 2007; Giordano et al., 2006; Gorelli et al., 2004; Iota and Yoo, 2001; Litasov et al., 2011; Teweldeberhan et al., 2013). Solid lines indicate a thermodynamic phase transition and the dashed lines indicate a kinetic transition. The orange line indicates the melting curve determined from *ab initio* simulations (Teweldeberhan et al., 2013). Coloured region indicates the P-T domain explored in this study and the extent to which polymerisation occurs (0-100%, blue to red).

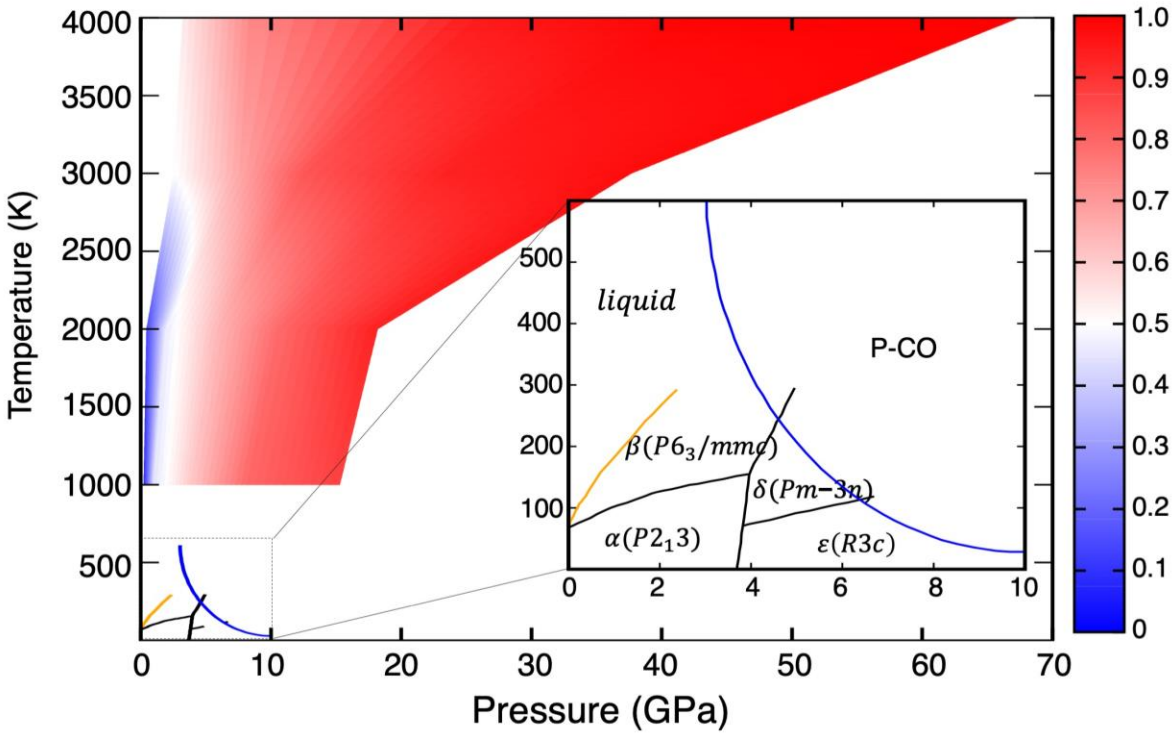

Figure 4. P-T phase diagram of CO. The black and orange lines show the phase boundaries (Cromer et al., 1983; Fukushima et al., 1977; Serdyukov et al., 2010). The blue line indicates the boundary between polymerised CO and the solid phases. The orange line represents the solid/liquid boundary. Coloured region indicates the extent to which polymerisation occurs (0-100%, blue to red).

3.2 EOS of CO and CO_2

As discussed above, the polymerisation of CO_2 can go up to 95% while still in the liquid field. Although some simulations extend into the solid phase field, they are metastable liquids and so are not used to fit the EOS. For CO, there is no melting information available at high P & T and so we neglected the data with 100% polymerisation in the fitting of EOS. In addition, we included the low P & T EOS data for CO_2 (up to 0.8 GPa and 1100 K) from Span and Wagner (1996) and EOS data for CO (up to 0.1 GPa and 1000 K) from Goodwin (1985) in the fitting, as low-pressure data is important for the accuracy of Gibbs free energy calculation. The data was fitted into a modified Lee-Kesler EOS, and the derived parameters are shown in Table 2. The obtained CO_2 EOS is valid from 298.15 to 4000 K and 1 bar to 70 GPa, and the CO EOS is valid from 298.15 to 4000 K and 1 bar to 40 GPa.

Table 2. Derived parameters for the modified Lee-Kesler EOSs (see eqs. (1-8)) of CO and CO_2 fluids. The uncertainty in pressure is less than 10% on average in the region studied.

Parameter	CO_2	CO

V_C (cm^3/mol)	94.0	92.166
T_C (K)	304.1	132.85
a_1	-0.060417280674	0.039835176862
a_2	29.312930805997	-2.543808448869
a_3	-26.741784606481	14.322113574972
a_4	0.582336809237	0.229238078128
a_5	-22.996326249305	-1.546458778437
a_6	-5.656015266431	-20.423296489026
a_7	-0.001944185691	-0.004813112395
a_8	2.276867190172	0.522356542096
a_9	-0.691325562713	1.397315140656
a_{10}	-0.000523527797	0.000336467163
a_{11}	-0.174510207149	-0.021999704023
a_{12}	-0.568501377298	-0.289945554888
α	-0.004054826576	-0.003542754107
β	-5328.542315117454	-3039.82823322819
γ	-0.047819433473	0.009093668377

4 Discussion

4.1 Comparison with previous EOS of CO and CO_2

Our EOS for CO_2 is compared in Figure 5 to those available in the literature, namely, BS-1992 (Belonoshko and Saxena, 1992), CG-2003 (Churakov and Gottschalk, 2003), DZ-2006 (Duan and Zhang, 2006), and FB-2017 (Fu et al., 2017). BS-1992 and CG-2003 are very similar, but they lie at lower pressures than both our results and FB-2017 for the same volumes. These two sets (BS-1992 and CG-2003) are based on a classical potential fitted to experimental data at low pressures. In contrast, DZ-2006 predicts the highest pressure among the five sets of EOS at the same volume. DZ-2006 was also obtained by MD based on molecular potentials determined under room temperature and pressure, and it was said to be valid in the temperature–pressure range from 673.15 to 2573.15 K up to 10.0 GPa. The final set discussed, FB-2017, was produced completely from AIMD simulations. Their calculated results are in good agreement with our results.

For CO fluids, we found one set of EOS data from classical MD simulations (BS-1991) (Belonoshko and Saxena, 1991b), and one set of EOS data based on AIMD simulations (Leonhardi-2017) (Leonhardi and Militzer, 2017). We plot them in Figure 6 together with our results and the shock-wave data from Nellis et al. (1981). It was shown by Nellis's experiment (Nellis et al., 1981) that the CO fluids with molar volume less than 13 cm^3/mol are all deeply polymerised or solidified. Nellis also suggested a dense solid carbon phase at these conditions. Our simulations also show a deeply polymerised CO with molar volume less than 13 cm^3/mol. So, our results agree with experiments in this regard. On the other hand, the Leonhardi-2017 EOS

shows a remarkable difference when compared to our results at high pressures (Leonhardi and Militzer, 2017). In this case, the difference in input structure should not affect the result as CO is more reactive and can be easily polymerised. The difference between our work and Leonhardi-2017 is hard to understand and must await further clarification.

The comparison above indicates that EOSs from classical potentials will suffer from being unable to successfully capture the bonding behaviour of these fluids. This can be understood from the analysis of the evolution of molecular bonding in CO and CO_2 fluids. There is a complex process involving the establishment of new bonds via intermolecular interaction and the decomposition of molecules, which cannot be described by classical models. Moreover, the extrapolation of any experimental data or theoretical calculations may also fail to capture structural changes.

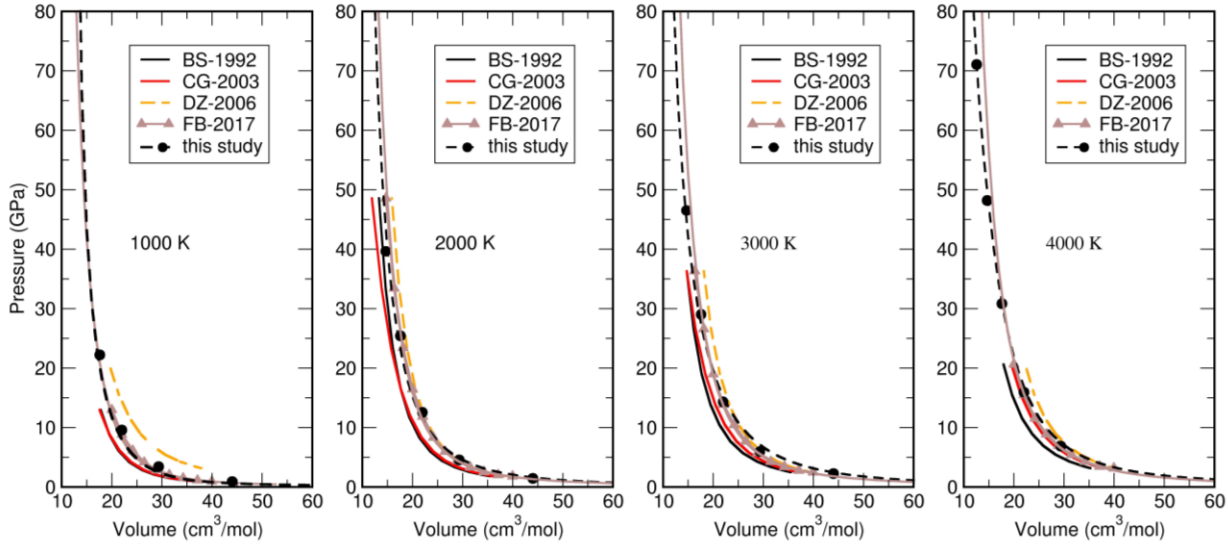

Figure 5. Derived EOS for CO_2 fluid in comparison with existing EOSs. BS-1992 EOS is from Belonoshko and Saxena (1992), CG-2003 EOS is from Churakov and Gottschalk (2003), DZ-2006 EOS is from Duan and Zhang (2006), and FB-2017 is from Fu et al. (2017).

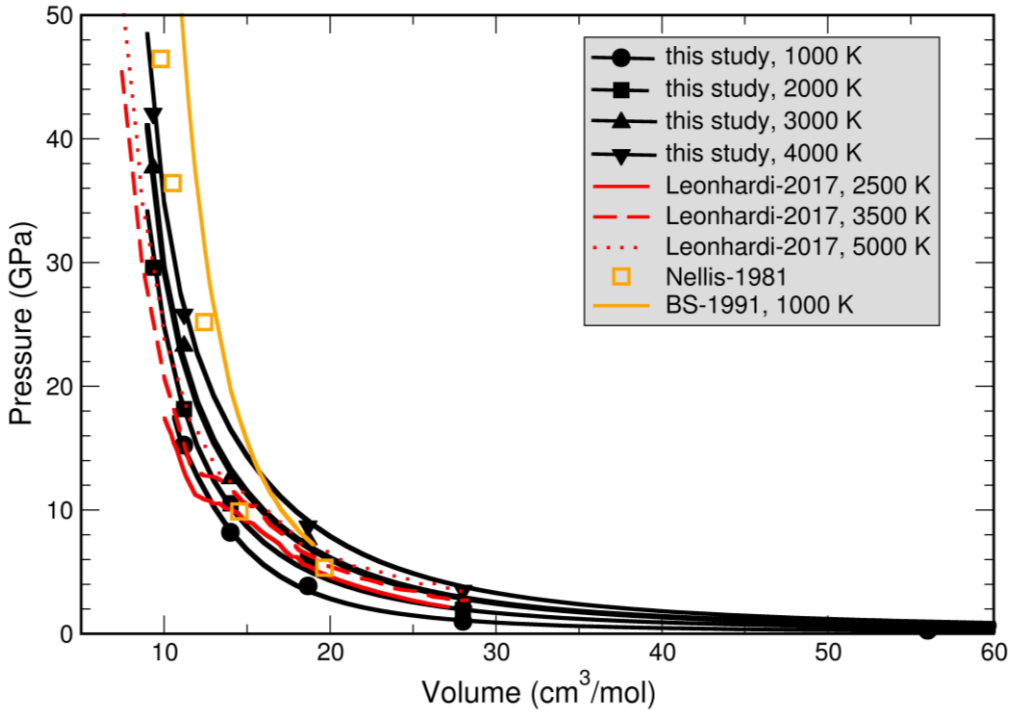

Figure 6. Derived EOS for the CO in comparison with existing EOSs and data. BS-1991 EOS is from Belonoshko and Saxena (1991b), Leonhardi-2017 EOS is from Leonhardi and Militzer (2017).

4.2 Stability of carbonates at Earth's mantle conditions

In order to test the equations of state further, we have used it to predict the decarbonation reactions of carbonates at high P and T. These reactions are important since carbonates like $MgCO_3$ and $CaCO_3$ are the main carbon-bearing minerals in subducting slabs that can be transported down to the transition zone or lower mantle. Decarbonation reactions do appear to occur, as inferred from diamonds originating from the mantle transition zone or the lower mantle. The presence of carbonate inclusions in "super-deep diamonds" indicates that decarbonation reactions may have a profound influence on mantle structure and the carbon cycle up to lower mantle conditions (Brenker et al., 2007; Walter et al., 2008). Many experimental and theoretical studies have been done to investigate the stability of $MgCO_3$ and $CaCO_3$ under a wide range of P & T (Drewitt et al., 2019; Litasov et al., 2008; Litasov et al., 2017; Maeda et al., 2017; Oganov et al., 2008; Santos et al., 2020; Zhang et al., 2018). However, in-depth analyses are often limited to low pressures due to the lack of reliable EOSs for CO and CO_2 fluids valid to high P & T. With our CO_2 EOS valid

in the P & T ranges of 0-70 GPa and 298.15-4000 K, we investigated the stability of $MgCO_3$ and $CaCO_3$ under various conditions.

$MgCO_3$ stabilises in the *magnesite* (*mgs*) phase below ~80 GPa, and above that transforms into *magnesite-II* (Isshiki et al., 2004; Maeda et al., 2017; Oganov et al., 2008). It can decompose into *periclase* MgO (*per*) and CO_2 upon heating. Redfern et al. (1993) applied their EOS for $MgCO_3$ up to 20 GPa and other thermodynamic data to the reaction (***R1***). They found that $MgCO_3$ is stable over MgO and CO_2 through the mantle, as can be seen in Figure 7a. Fiquet et al. (2002) estimated the stability of $MgCO_3$ based on their ambient EOS of $MgCO_3$ and a likely range of $(\partial B_0/\partial T)_p$. As shown in Figure 7a, the equilibrium line of reaction (***R1***) determined by Fiquet et al. (2002) lies below those of Redfern et al. (1993) below ~4 GPa, and goes above those of Redfern et al. (1993) between ~4-16 GPa. $(\partial B_0/\partial T)_p$ does not make much difference below ~10 GPa, and above that the equilibrium line strongly depends on $(\partial B_0/\partial T)_p$. Litasov et al. (2008) determined the EOS of *magnesite* up to 32 GPa and 2073 K. By integrating their EOS and the CO_2 EOS of Belonoshko and Saxena (1991b) in the thermodynamic model, they confirmed the stability of $MgCO_3$ at mantle conditions. We used the EOSs of $MgCO_3$ and MgO from Litasov et al. (2008) and the EOS of CO_2 determined above to calculate the Gibbs free energy of reaction (***R1***). As can be seen in Figure 7a, our result agrees well with that of Litasov et al. (2008). It also agrees well with that of Fiquet et al. (2002) below ~10 GPa. The equilibrium lines of Redfern et al. (1993) have a slightly different slope, and this could be due to the use of volume-independent Anderson-Gruneisen parameter. Regardless, $MgCO_3$ is always found to be stable relative to MgO + CO_2 fluid under mantle conditions.

The reaction of $MgCO_3$ with SiO_2 (reaction (***R2***)) was also considered as SiO_2 is a major component in subducted slabs. SiO_2 stabilises mainly in the *α-quartz*, *β-quartz*, *coesite* and *stishovite* phases from low to high pressures (Swamy et al., 1994). The product $MgSiO_3$ also has a rich phase diagram, but the dominant phases are the *orthoenstatite* and *perovskite* phases (Litasov and Shatskiy, 2019; Tomioka et al., 2016). We included all the mentioned structures in the thermodynamic calculation of reaction (***R2***). As can be seen in Figure 7b, our result agrees well with the experimental data at 0–4 GPa. However, the equilibrium line of Litasov et al. (2008) shows a different slope from ours, possibly because they used the CO_2 EOS of Belonoshko and Saxena (1991b), which produces a smaller volume than ours at the same pressure and that stabilises

CO_2. Nevertheless, these studies suggest the stability of $MgCO_3$ + SiO_2 over $MgSiO_3$ + CO_2 fluid under mantle conditions.

Figure 7b shows a number of other decarbonation reactions from the literature which are relevant. For instance, above around ~8 GPa, the experiments of Litasov and Shatskiy (2019) (solid yellow line) and Kakizawa et al. (2015) (solid green line) show a change in the slope of the ***R2*** decarbonation reaction, with it occurring at much lower temperatures than we predict. This is likely due to partial melting of $MgCO_3$ + SiO_2 occurring before the decarbonation reaction ***R2***; however we do not yet model the melts and cannot test this.

Recent experiments by Maeda et al. (2017) found that diamond can form from the reaction of $MgCO_3$ and SiO_2 at deep lower mantle conditions following the reaction

(***R5***) $$MgCO_3 + SiO_2 = MgSiO_3 + C + O_2$$

Similarly, Drewitt et al. (2019) also find a decarbonation reaction at higher pressures, although not always associated with diamond formation. These conditions lie in the solid region of CO_2 and so are also beyond the predictability of our thermodynamic model. However, the low pressure end of the equilibrium line of (***R5***) determined by Maeda et al. (2017) is predicted to meet the melting curve of CO_2 at *ca*. 40 GPa and 2100 K, where our calculated ΔG_r is *ca*. 140 kJ/mol. This means that reaction (***R2***) cannot occur at *ca*. 40 GPa and 2100 K even if CO_2 is in the solid state, but can only occur further into the solid field where the free energy difference between solid and liquid CO_2 overcomes ΔG_r of (***R2)*** shown in Figure 7b. According to the Gibbs free energies calculated by Teweldeberhan et al. (2013), the pressure needs to be ~11 GPa higher than the melting curve for solid CO_2 to be more stable than the fluid by 140 kJ/mol. When considering the uncertainty in the free energies here and in Teweldeberhan et al. (2013), the majority of the high pressure decarbonation reaction of Maeda et al (2017) and Drewitt et al. (2019) are consistent with this. Alternatively, high-pressure decarbonation may be powered by the formation of diamond via CO_2 = C + O_2, however, some of the decarbonation reactions seen by Drewitt et al (2019) do not produce diamond. Unfortunately, we do not have suitable equations of state for this reaction to test this. Finally, if $MgCO_3$ can become unstable in the presence of SiO_2, then $MgCO_3$ is also expected to be unstable in the absence of SiO_2, given that the Gibbs free energy change is similar for both reactions (***R1***) and (***R2***).

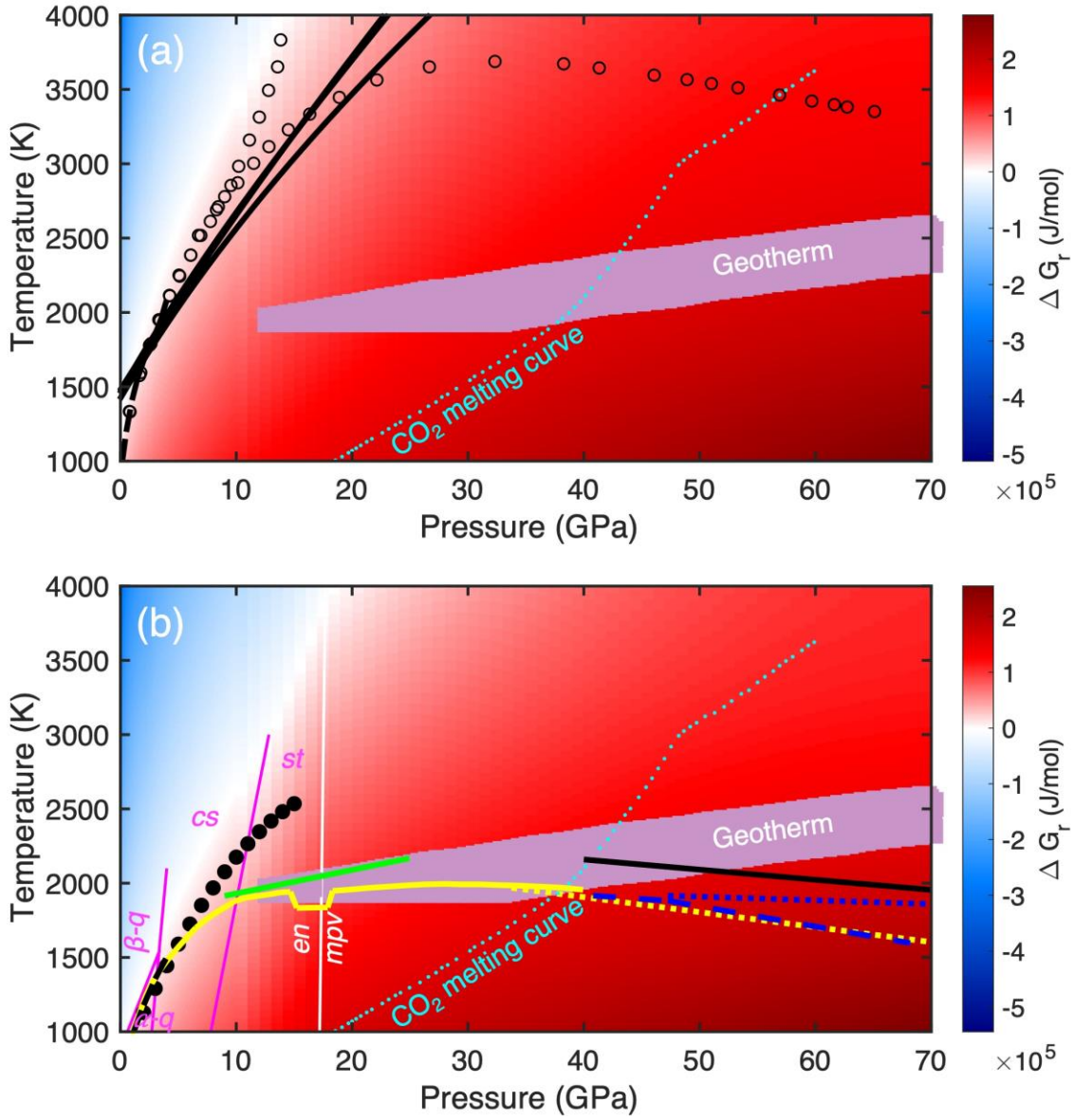

Figure 7. (a) Gibbs free energy of $MgCO_3 = MgO + CO_2$ calculated using the CO_2 EOS from this work. Also shown are various phases boundaries from the literature. Black solid curve is the phase boundary calculated by Redfern et al. (1993) and the black dashed curve is experimental phase boundary from Litasov et al. (2008). The black open circles are from thermodynamic calculations of Fiquet et al. (2002), with the ones at higher temperatures using $(\partial B_0/\partial T)_p = -0.021$ GPa/K and the other ones using $(\partial B_0/\partial T)_p = -0.013$ GPa/K. The CO_2 melting curve (dotted cyan) determined by *ab initio* simulations is from Teweldeberhan et al. (2013). (b) Gibbs free energy of $MgCO_3 + SiO_2 = MgSiO_3 + CO_2$ calculated using CO_2 EOS from this work. The dashed black curve is the phase boundary from Haselton Jr et al. (1978) and Koziol and Newton (1995). The filled black circles are from the thermodynamic calculations of from Litasov et al. (2008). Solid yellow curve is from experiment of Litasov and Shatskiy (2019). Solid green line is from experiment of Kakizawa et al. (2015). The dashed blue line is from experiments of Drewitt et al. (2019). The solid black line is from experiment of Maeda et al. (2017). Yellow dotted and blue

dotted lines are the CO_2 (s) = C+O_2 boundary from Litasov et al. (2011) and Drewitt et al. (2019), respectively. Magenta lines indicate the calculated phase boundaries for *α-quartz* (*α-q*), *β-quartz* (*β--q*), *coesite* (*cs*) and *stishovite* (*st*). The white line indicates the calculated phase boundary between the *orthoenstatite* and *perovskite* (*mpv*) $MgSiO_3$.

$CaCO_3$ has a complex phase diagram and experiences several phases transformations from low to high pressures. Recently, Zhang et al. (2018) have thoroughly investigated the stability of different polymorphs of $CaCO_3$, which include the *aragonite*, $CaCO_3$-*P*2_1/*c*-*l* (*l* denotes low pressure), *postaragonite*, $CaCO_3$-*P*21/*c*-*h* (*h* denotes high pressure), $CaCO_3$-*Pnma*-*h*, $CaCO_3$-VI, and pyroxene-type phases. We also include all these phases in our thermodynamic calculations. For CaO, we considered the *quicklime* phase. We used the experimental EOS for *aragonite* and *quicklime*, and *ab initio* EOS from Zhang et al. (2018) for other $CaCO_3$ phases. As can be seen in Figure 8a, our result shows that $CaCO_3$ is stable over CaO + CO_2 fluid under mantle conditions. The change of Gibbs free energy of reaction (***R3***) along the melting curve of CO_2 is about 200 kJ/mol, which is in excellent agreement with *ab initio* calculations of Santos et al. (2019), who calculated the decomposition of $CaCO_3$ into CaO and solid CO_2.

$CaCO_3$ is less stable in the presence of SiO_2, as can be seen in Figure 8b. In the thermodynamic calculation of reaction (***R4***), we considered four stable phases for $CaSiO_3$, namely, the *wollastonite-I*, *wollastonite-II*, *pseudowollastonite* and *perovskite* phases. Our result agrees well with the experimental data at 0-0.5 GPa from Harker and Tuttle (1956) and the thermodynamic calculation of Litasov et al. (2017) up to 12 GPa. Our result together with these studies consistently suggests the stability of $CaCO_3$ over $CaSiO_3$ under upper mantle conditions. Recent experiment by Li et al. (2018) observed decarbonation in reaction (***R4***) and suggest that $CaCO_3$ is unstable in the presence of SiO_2 at conditions from ~25 to 60 GPa and from ~1200 to 1600 K. Such conditions are also in the domain of solid CO_2 and beyond the predictability of our thermodynamic model. Nevertheless, our calculated ΔG_r for reaction (***R4***) along the equilibrium line of Li et al. (2018) is about 150 kJ/mol, which is comparable to our calculated ΔG_r of ~150 kJ/mol for (***R2***) along the experimentally determined equilibrium line of (***R5***); So, it is likely that the transformation of $CaCO_3$ into $CaSiO_3$ is also driven by the partial melting of carbonate or by the diamond formation from CO_2.

To summarize this part, our results agree with available experimental and theoretical studies performed at low pressures. Our results indicate the stability of both $MgCO_3$ and $CaCO_3$ pure phases at upper mantle conditions with or without the presence of SiO_2. Both $MgCO_3$ and $CaCO_3$ may become unstable at deeper mantle conditions, and the decarbonation is likely to be driven by the formation of diamond or partial melting of carbonate.

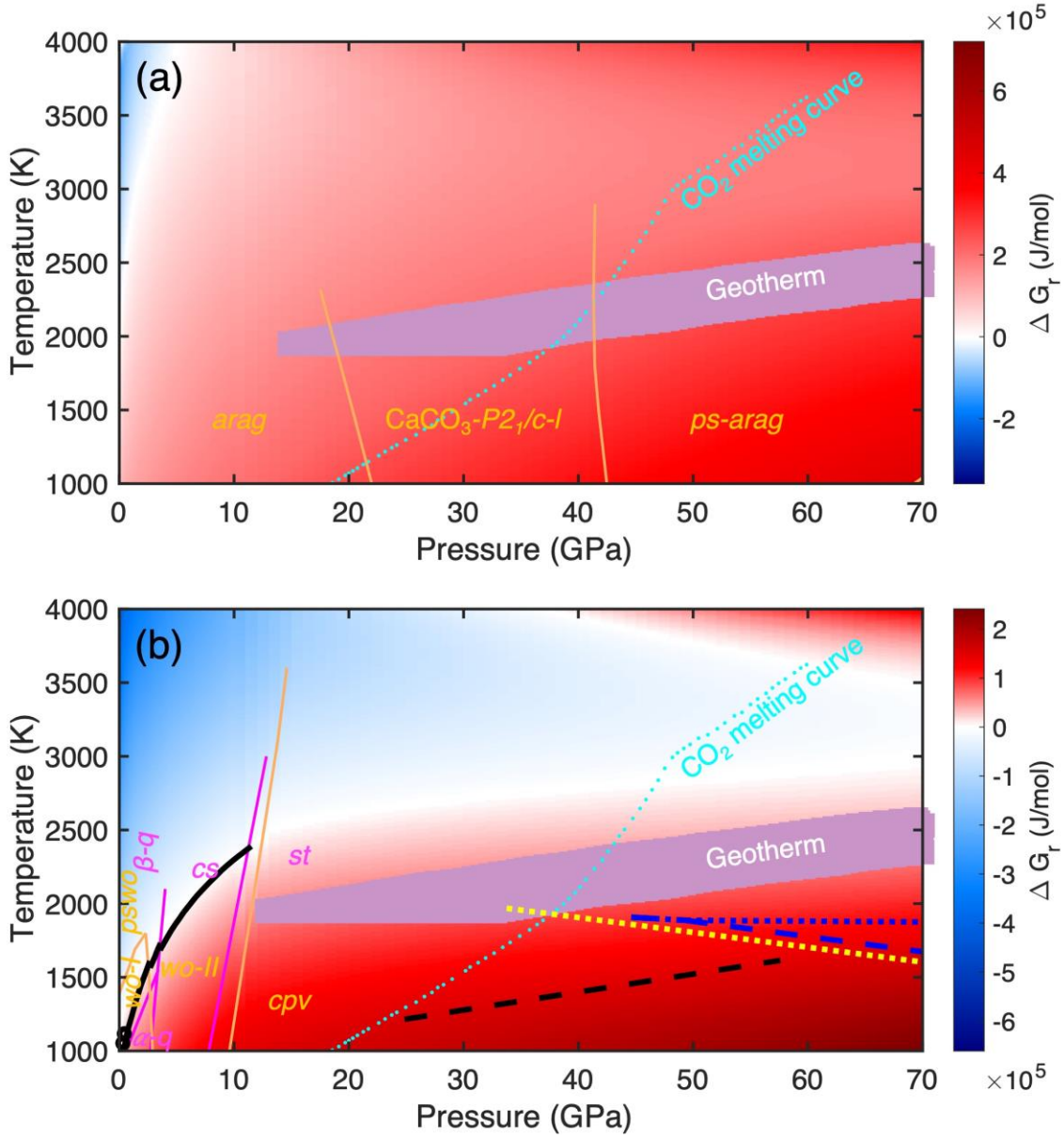

Figure 8. (a) Gibbs free energy of $CaCO_3 = CaO + CO_2$ calculated using our CO_2 EOS from this work. Orange lines show the phase boundaries between the *aragonite* (*arag*), $CaCO_3$-*P*2_1/*c*-*I* and *postaragonite* (*ps-arag*) phases. The CO_2 melting curve (dotted cyan) determined by *ab initio* simulations is from Teweldeberhan et al. (2013). (b) Gibbs free energy of $CaCO_3 + SiO_2 = CaSiO_3 + CO_2$ calculated using the CO_2 EOS from this work. Empty back circles are experimental data from Harker and Tuttle (1956), solid black curve is thermodynamic calculation from Litasov

et al. (2017), and the dashed black curve is experimental data from Li et al. (2018). The dashed blue line is from experiments of Drewitt et al. (2019). Yellow dotted and blue dotted lines are the CO_2 (s) = C+O_2 boundary from Litasov et al. (2011) and Drewitt et al. (2019), respectively. Magenta lines indicate the calculated phase boundaries for *α-quartz* (*α-q*), *β-quartz* (*β--q*), *coesite* (*cs*) and *stishovite* (*st*). Orange lines show the phase boundaries between the *wollastonite-I* (*wo-I*), *wollastonite-II* (*wo-I*), *pseudowollastonite* (*pswo*) and *perovskite* (*cpv*) $CaSiO_3$.

5 Conclusions

We have obtained EOSs for CO and CO_2 fluids by performing AIMD simulations, which are valid in the ranges of 1 bar to 40 GPa and 298.15 to 4000 K for CO, and 1 bar to 70 GPa and 298.15 to 4000 K for CO_2. We found that both CO and CO_2 fluids polymerise via the establishment of intermolecular bonding, while the intramolecular bonding is generally unaffected. Polymerisation is found to be a pressure-driven process, starting at very low pressures. These findings suggest a more complex bonding evolution than previously thought, and therefore extrapolations from either low-pressure experimental data or from theoretical calculations using empirical potentials must be treated with caution. The derived CO_2 EOS was applied to decarbonation reactions of both $MgCO_3$ and $CaCO_3$. Our thermodynamic calculations reproduced the experimental results and agree well with other thermodynamic calculations at low pressures. Both $MgCO_3$ and $CaCO_3$ pure phases are found to be stable with or without SiO_2 at upper mantle conditions, but they may become unstable approaching the lower mantle.

Acknowledgments

This work was supported by NERC grant NE/M000125/1. Calculations were partly performed using the ARCHER supercomputer facility. We also acknowledge use of the NEXCS system, a collaborative facility supplied under the Joint Weather and Climate Research Programme, a strategic partnership between the Met Office and the Natural Environment Research Council. The authors declare no conflicts of interest.

Data availability

The data are already included in the manuscript as Tables 1 and 2.

Appendix A. Supplementary data

Supplementary data to this article can be found online.

References

Belonoshko, A., Saxena, S.K., 1991a. A molecular dynamics study of the pressure-volume-temperature properties of super-critical fluids: I. H2O. Geochim. Cosmochim. Acta 55, 381-387.

Belonoshko, A., Saxena, S.K., 1991b. A molecular dynamics study of the pressure-volume-temperature properties of supercritical fluids: II. CO_2, CH_4, CO, O_2, and H_2. Geochim. Cosmochim. Acta 55, 3191-3208.

Belonoshko, A.B., Saxena, S.K., 1992. A unified equation of state for fluids of C-H-O-N-S-Ar composition and their mixtures up to very high temperatures and pressures. Geochim. Cosmochim. Acta 56, 3611-3626.

Bernard, S., Chiarotti, G.L., Scandolo, S., Tosatti, E., 1998. Decomposition and polymerization of solid carbon monoxide under pressure. Phys. Rev. Lett. 81, 2092-2095.

Blöchl, P.E., 1994. Projector augmented-wave method. Phys. Rev. B 50, 17953.

Brenker, F.E., Vollmer, C., Vincze, L., Vekemans, B., Szymanski, A., Janssens, K., Szaloki, I., Nasdala, L., Joswig, W., Kaminsky, F., 2007. Carbonates from the lower part of transition zone or even the lower mantle. Earth Planet. Sci. Lett. 260, 1-9.

Cavazzoni, C., Chiarotti, G.L., Scandolo, S., Tosatti, E., Bernasconi, M., Parrinello, M., 1999. Superionic and metallic states of water and ammonia at giant planet conditions. Science 283, 44-44.

Chopelas, A., Boehler, R., 1992. Thermal expansivity in the lower mantle. Geophys. Res. Lett. 19, 1983-1986.

Churakov, S.V., Gottschalk, M., 2003. Perturbation theory based equation of state for polar molecular fluids: I. Pure fluids. Geochim. Cosmochim. Acta 67, 2397-2414.

Cromer, D.T., Schiferl, D., LeSar, R., Mills, R.L., 1983. Room-temperature structure of carbon monoxide at 2.7 and 3.6 GPa. Acta Crystallogr. C 39, 1146-1150.

Datchi, F., Giordano, V.M., Munsch, P., Saitta, A.M., 2009. Structure of carbon dioxide phase IV: Breakdown of the intermediate bonding state scenario. Phys. Rev. Lett. 103, 185701-185701.

Di Tolla, F.D., Ronchetti, M., 1993. Applicability of Nosé isothermal reversible dynamics. Phys. Rev. B 48, 1726.

Drewitt, J.W.E., Walter, M.J., Zhang, H., McMahon, S.C., Edwards, D., Heinen, B.J., Lord, O.T., Anzellini, S., Kleppe, A.K., 2019. The fate of carbonate in oceanic crust subducted into Earth's lower mantle. Earth Planet. Sci. Lett. 511, 213-222.

Duan, Z., Zhang, Z., 2006. Equation of state of the H_2O, CO_2, and H_2O–CO_2 systems up to 10 GPa and 2573.15K: Molecular dynamics simulations with *ab initio* potential surface. Geochim. Cosmochim. Acta 70, 2311-2324.

Dubrovinsky, L.S., Swamy, V., 1997. Thermodynamic data for the phases in the $CaSiO_3$ system. Geochim. Cosmochim. Acta 61, 1181-1191.

Fiquet, G., Guyot, F., Kunz, M., Matas, J., Andrault, D., Hanfland, M., 2002. Structural refinements of magnesite at very high pressure. Am. Mineral. 87, 1261-1265.

Fu, J., Zhao, J., Plyasunov, A.V., Belonoshko, A.B., 2017. *Ab initio* molecular dynamics study of fluid H_2O-CO_2 mixture in broad pressure-temperature range. AIP Adv. 7, 115217-115217.

Fukushima, E., Gibson, A.A.V., Scott, T.A., 1977. Carbon‐13 NMR of carbon monoxide. I. Pressure dependence of translational motion in β-CO. J. Chem. Phys. 66, 4811-4817.

Giordano, V.M., Datchi, F., 2007. Molecular carbon dioxide at high pressure and high temperature. Europhys. Lett. 77, 46002.

Giordano, V.M., Datchi, F., Dewaele, A., 2006. Melting curve and fluid equation of state of carbon dioxide at high pressure and high temperature. J. Chem. Phys. 125, 54504-54504.
Goodwin, R.D., 1985. Carbon monoxide thermophysical properties from 68 to 1000 K at pressures to 100 MPa. J. Phys. Chem. Ref. Data 14, 849-932.
Gorelli, F.A., Giordano, V.M., Salvi, P.R., Bini, R., 2004. Linear carbon dioxide in the high-pressure high-temperature crystalline phase IV. Phys. Rev. Lett. 93, 205503-205503.
Harker, R.I., Tuttle, O.F., 1956. Experimental data on the Pco_2-T curve for the reaction: calcite+quartz=wollastonite+carbon dioxide. Am. J. Sci. 254, 239-256.
Haselton Jr, H.T., Sharp, W.E., Newton, R.C., 1978. CO_2 fugacity at high temperatures and pressures from experimental decarbonation reactions. Geophys. Res. Lett. 5, 753-756.
Hubbard, W.B., 1981. Interiors of the giant planets. Science 214, 145-145.
Iota, V., Yoo, C.-S., 2001. Phase diagram of carbon dioxide: Evidence for a new associated phase. Phys. Rev. Lett. 86, 5922-5925.
Iota, V., Yoo, C.-S., Klepeis, J.-H., Jenei, Z., Evans, W., Cynn, H., 2006. Six-fold coordinated carbon dioxide VI. Nat. Mater. 6, 34.
Isshiki, M., Irifune, T., Hirose, K., Ono, S., Ohishi, Y., Watanuki, T., Nishibori, E., Takata, M., Sakata, M., 2004. Stability of magnesite and its high-pressure form in the lowermost mantle. Nature 427, 60-63.
Kakizawa, S., Inoue, T., Suenami, H., Kikegawa, T., 2015. Decarbonation and melting in $MgCO_3$–SiO_2 system at high temperature and high pressure. Journal of Mineralogical and Petrological Sciences 110, 179-188.
Koziol, A.M., Newton, R.C., 1995. Experimental determination of the reactions magnesite + quartz = enstatite + CO_2 and magnesite = periclase + CO_2, and enthalpies of formation of enstatite and magnesite. Am. Mineral. 80, 1252-1260.
Kresse, G., Furthmüller, J., 1996. Efficiency of ab-initio total energy calculations for metals and semiconductors using a plane-wave basis set. Comput. Mater. Sci. 6, 15-50.
Kresse, G., Hafner, J., 1993. *Ab initio* molecular dynamics for open-shell transition metals. Phys. Rev. B 48, 13115.
Kresse, G., Joubert, D., 1999. From ultrasoft pseudopotentials to the projector augmented-wave method. Phys. Rev. B 59, 1758.
Lee Byung, I., Kesler Michael, G., 1975. A generalized thermodynamic correlation based on three-parameter corresponding states. AIChE J. 21, 510-527.
Leonhardi, T.C., Militzer, B., 2017. *Ab initio* simulations of liquid carbon monoxide at high pressure. High Energ. Dens. Phys. 22, 41-45.
Li, X., Zhang, Z., Lin, J.-F., Ni, H., Prakapenka, V.B., Mao, Z., 2018. New high-pressure phase of $CaCO_3$ at the topmost lower mantle: Implication for the deep-mantle carbon transportation. Geophys. Res. Lett. 45, 1355-1360.
Litasov, K.D., Fei, Y., Ohtani, E., Kuribayashi, T., Funakoshi, K., 2008. Thermal equation of state of magnesite to 32 GPa and 2073 K. Phys. Earth Planet. Inter. 168, 191-203.
Litasov, K.D., Goncharov, A.F., Hemley, R.J., 2011. Crossover from melting to dissociation of CO_2 under pressure: Implications for the lower mantle. Earth Planet. Sci. Lett. 309, 318-323.
Litasov, K.D., Shatskiy, A., Gavryushkin, P.N., Bekhtenova, A.E., Dorogokupets, P.I., Danilov, B.S., Higo, Y., Akilbekov, A.T., Inerbaev, T.M., 2017. P-V-T equation of state of $CaCO_3$ aragonite to 29 GPa and 1673 K: In situ X-ray diffraction study. Phys. Earth Planet. Inter. 265, 82-91.

Litasov, K.D., Shatskiy, A.F., 2019. $MgCO_3$ + SiO_2 Reaction at Pressures up to 32 GPa Studied Using in-Situ X-Ray Diffraction and Synchrotron Radiation. Geochem. Int. 57, 1024-1033.
Maeda, F., Ohtani, E., Kamada, S., Sakamaki, T., Hirao, N., Ohishi, Y., 2017. Diamond formation in the deep lower mantle: a high-pressure reaction of $MgCO_3$ and SiO_2. Sci. Rep. 7, 40602-40602.
Martínez, L., Andrade, R., Birgin, E.G., Martínez, J.M., 2009. PACKMOL: a package for building initial configurations for molecular dynamics simulations. J. Comput. Chem. 30, 2157-2164.
Nellis, W.J., Mitchell, A.C., Ree, F.H., Ross, M., Holmes, N.C., Trainor, R.J., Erskine, D.J., 1991. Equation of state of shock‐compressed liquids: Carbon dioxide and air. J. Chem. Phys. 95, 5268-5272.
Nellis, W.J., Ree, F.H., van Thiel, M., Mitchell, A.C., 1981. Shock compression of liquid carbon monoxide and methane to 90 GPa (900 kbar). J. Chem. Phys. 75, 3055-3063.
Nosé, S., 1984. A unified formulation of the constant temperature molecular dynamics methods. J. Chem. Phys. 81, 511-519.
Oda, H., Anderson, O.L., Isaak, D.G., Suzuki, I., 1992. Measurement of elastic properties of single-crystal CaO up to 1200 K. Phys. Chem. Miner. 19, 96-105.
Oganov, A.R., Ono, S., Ma, Y., Glass, C.W., Garcia, A., 2008. Novel high-pressure structures of $MgCO_3$, $CaCO_3$ and CO_2 and their role in Earth's lower mantle. Earth Planet. Sci. Lett. 273, 38-47.
Perdew, J.P., Burke, K., Ernzerhof, M., 1996. Generalized Gradient Approximation Made Simple. Phys. Rev. Lett. 77, 3865--3868.
Redfern, S.A.T., Wood, B.J., Henderson, C.M.B., 1993. Static compressibility of magnesite to 20 GPa: Implications for $MgCO_3$ in the lower mantle. 20, 2099-2102.
Santoro, M., Gorelli, F.A., 2006. High pressure solid state chemistry of carbon dioxide. Chem. Soc. Rev. 35, 918-931.
Santos, S.S.M., Marcondes, M.L., Justo, J.F., Assali, L.V.C., 2019. Stability of calcium and magnesium carbonates at Earth's lower mantle thermodynamic conditions. Earth Planet. Sci. Lett. 506, 1-7.
Santos, S.S.M., Marcondes, M.L., Justo, J.F., Assali, L.V.C., 2020. Calcium carbonate at high pressures and high temperatures: A first-principles investigation. Phys. Earth Planet. Inter. 299, 106327.
Serdyukov, A., Vetter, M., Brodyanski, A., Jodl, H.J., 2010. Lattice phonons of solid phases (α,β,δ,ε) of carbon monoxide by optical studies. Low Temp. Phys. 36, 424-438.
Span, R., Wagner, W., 1996. A new equation of state for carbon dioxide covering the fluid region from the triple-point temperature to 1100 K at pressures up to 800 MPa. J. Phys. Chem. Ref. Data 25, 1509-1596.
Swamy, V., Saxena, S.K., Sundman, B., Zhang, J., 1994. A thermodynamic assessment of silica phase diagram. J. Geophys. Res.:Solid Earth 99, 11787-11794.
Tange, Y., Kuwayama, Y., Irifune, T., Funakoshi, K.-i., Ohishi, Y., 2012. P-V-T equation of state of $MgSiO_3$ perovskite based on the MgO pressure scale: A comprehensive reference for mineralogy of the lower mantle. J. Geophys. Res.:Solid Earth 117, B06201.
Teweldeberhan, A.M., Boates, B., Bonev, S.A., 2013. CO_2 in the mantle: Melting and solid–solid phase boundaries. Earth Planet. Sci. Lett. 373, 228-232.
Tomioka, N., Miyahara, M., Ito, M., 2016. Discovery of natural $MgSiO_3$ tetragonal garnet in a shocked chondritic meteorite. Sci. Adv. 2, e1501725.

Walter, M.J., Bulanova, G.P., Armstrong, L.S., Keshav, S., Blundy, J.D., Gudfinnsson, G., Lord, O.T., Lennie, A.R., Clark, S.M., Smith, C.B., Gobbo, L., 2008. Primary carbonatite melt from deeply subducted oceanic crust. Nature 454, 622-625.
Zhang, Z., Mao, Z., Liu, X., Zhang, Y., Brodholt, J., 2018. Stability and reactions of $CaCO_3$ polymorphs in the Earth's deep mantle. J. Geophys. Res.:Solid Earth 123, 6491-6500.